

REPORT DOCUMENTATION PAGE

The public reporting burden for this collection of information is estimated to average 1 hour per response, including the time for reviewing instructions, searching existing data sources, gathering and maintaining the data needed, and completing and reviewing the collection of information. Send comments regarding this burden estimate or any other aspect of this collection of information, including suggestions for reducing the burden, to the Department of Defense, Executive Services and Communications Directorate (0704-0188). Respondents should be aware that notwithstanding any other provision of law, no person shall be subject to any penalty for failing to comply with a collection of information if it does not display a currently valid OMB control number.

PLEASE DO NOT RETURN YOUR FORM TO THE ABOVE ORGANIZATION.

1. REPORT DATE (DD-MM-YYYY) 12 NOV 2008		2. REPORT TYPE Final		3. DATES COVERED (From - To) 01 MAY 2005 to 30 APR 2008	
4. TITLE AND SUBTITLE (DURIP-05) DEEP ULTRAVIOLET LASER IMAGING FOR BIOLOGY				5a. CONTRACT NUMBER	
				5b. GRANT NUMBER FA9550-05-1-0285	
				5c. PROGRAM ELEMENT NUMBER	
6. AUTHOR(S) DR. DANIEL EHRLICH				5d. PROJECT NUMBER	
				5e. TASK NUMBER	
				5f. WORK UNIT NUMBER	
7. PERFORMING ORGANIZATION NAME(S) AND ADDRESS(ES) CENTER FOR BIOMEDICAL ENGINEERING MASSACHUSETTS INSTITUTE OF TECHNOLOGY NINE CAMBRIDGE CENTER, ROOM 661, CAMBRIDGE, MA 02142				8. PERFORMING ORGANIZATION REPORT NUMBER	
9. SPONSORING/MONITORING AGENCY NAME(S) AND ADDRESS(ES) AF OFFICE OF SCIENTIFIC RESEARCH /NE 875 NORTH RANDOLPH STREET ROOM 3112 ARLINGTON VA 22203				10. SPONSOR/MONITOR'S ACRONYM(S)	
				11. SPONSOR/MONITOR'S REPORT NUMBER(S)	
12. DISTRIBUTION/AVAILABILITY STATEMENT UNLIMITED					
13. SUPPLEMENTARY NOTES					
14. ABSTRACT The proposed research instrumentation will allow for greatly enhanced scope and efficiency of the ongoing programs, which have many important Air Force applications, particularly in monitoring hazardous materials, in health monitoring, and in fast forensic identification. The objective of this research instrumentation is to provide for the enhancement and augmentation of ongoing research in the area of laser photo chemistry. Research instrumentation will be procured to enhance and augment ongoing programs in biomolecular species identification. The funding will allow purchase of a ultraviolet laser system, which will be used for study of rapid direct detection and evaluation of genetic and molecular material in large parallel micro arrays.					
15. SUBJECT TERMS					
16. SECURITY CLASSIFICATION OF:			17. LIMITATION OF ABSTRACT	18. NUMBER OF PAGES	19a. NAME OF RESPONSIBLE PERSON DR. DANIEL EHRLICH
a. REPORT	b. ABSTRACT	c. THIS PAGE			19b. TELEPHONE NUMBER (Include area code) 617-258-7283

6897902

Final Technical Progress Report

"Deep Ultraviolet Laser Imaging for Biology"

Contract Number: FA 9550-05-1-0285

submitted by

Daniel Ehrlich, Principal Investigator
Massachusetts Institute of Technology
77 Massachusetts Ave.
Cambridge, MA 02139
ehrich@wi.mit.edu
(617) 258-7283

Administrative Contact
Amanda Tat
atat@mit.edu
(617) 253-2848

Period of Performance:
1 May 2005 to 1 May 2008

Date of Submission:
15 August 2008

20090312181

1 Overview and Status

This describes the status of a program to design and construct a deep-UV microscope for biological applications.

We have completed the design of a deep-UV confocal microscope in collaboration with an equipment vendor (Microcosm Corp.), have taken delivery of a frequency-doubled argon ion laser (Lexel Model 85-SHG), a q-switched microlaser (JDS Uniphase), and a custom designed final objective optic (Tropel Corporation). MIT has constructed a specialized beam expander and has provided it, with these new sources to the system integrator. We have also developed custom test samples (phalloidin-dyed and native actin fiber samples), and have debugged and refabricated the custom-fabricated deep uv optics that have been retrofitted into a commercial Zeiss microscope. The system is designed to retain its previous capability as a laser scanning microscope (LSM) in the visible but also to extend to LSM operation at 257 nm and 266 nm. The vendor Microcosm was slowed somewhat by the difficulty of the optical design in the deep UV, but the task has now been completed. MIT has taken delivery of the system and it has passed all of it's important quality testing.

In parallel, a wide-field deep-UV microscope system using deep UV LED sources was constructed. A high-frequency custom driving circuit was designed and built for the LED sources and tested for short pulse synchronized illumination with a CCD camera detector. A UV sensitive backthinned CCD camera was obtained from the vendor Princeton instruments and this system was used to test live cell imaging applications.

The surprising result that, not only fixed cells, but also live cells can be imaged in motility and cell division was discovered. We also proved that a unique kind of "quantitative" microscopy can be obtained at the new wavelengths of our system. These results published in the journal Nature Methods (Zeskind BJ, Jordan CD, Timp W., Trapani L, Waller G, Horodincu V, Ehrlich DJ, and Matusudaira P: **Nucleic acid and protein mass mapping by live-cell deep-ultraviolet microscopy**. Nature Methods 4(7); 567-569, 2007.) and are summarized below:

The foundation for a proof of concept lies on the ability to image at deep UV wavelengths. As described in (Zeskind, 2007) we have developed a deep UV microscope capable of measuring the summed contributions to 280 nm absorbance from nucleic acid (RNA and DNA) and protein. Compared to phase contrast and DIC (Fig. 2) images at visible wavelengths, a 280 nm image of fixed unlabeled cells (Fig. 3a) shows very good detail in cell structure with a distinct nucleus and nucleolus, a reticular cytoplasm, prominent retraction fibers, and concentrated mass at the leading edge membrane. Images of the native fluorescence of tryptophan from 280 nm excitation (Fig. 3b) measure protein concentration and quantum yield, revealing a continuous mass of protein throughout the cell with little distinction between the nucleus and the cytoplasm. Images acquired at 280nm have much higher spatial resolution than images acquired at visible wavelengths,

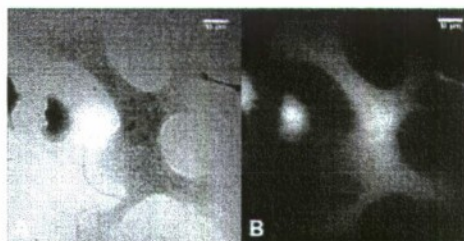


Fig. 4: Spatial resolution comparison using 205.6 nm beads imaged with (A) 280nm excitation and (B) 480nm excitation.

Images of the native fluorescence of tryptophan from 280 nm excitation (Fig. 3b) measure protein concentration and quantum yield, revealing a continuous mass of protein throughout the cell with little distinction between the nucleus and the cytoplasm. Images acquired at 280nm have much higher spatial resolution than images acquired at visible wavelengths,

as we have shown with 205.6nm beads (**Fig. 4**). The practical limit of resolution at 280 nm is 166 nm (for a 1.25NA objective and a 0.8NA condenser).

Although UV toxicity has hampered previous applications of UV microscopy in live cell imaging, we have drastically reduced UV exposure to 100 ms with a ~1 mW deep UV light-emitting-diode (LED) synchronized with a UV-coated back-illuminated CCD camera. Consequently, we are able to image dynamic cellular processes including mitosis (**Fig. 5a-f**) and motility (**Fig. 5g-i**). The mitosis images capture the chromosomes separating with high contrast and spatial resolution. The motility images show the ruffling region at the leading edge of the cell and the retraction fibers at the trailing edge. With 100 ms exposures we are able to image living cells for over six hours without visible harm, a dramatic improvement over 10 second exposures which rapidly cause necrosis. Although 100 ms exposures may still cause some amount of photodamage during longer-term studies, we detect no visible changes in cell dynamics or structure during shorter-term studies of processes such as motility and mitosis.

The key advantage of deep UV microscopy is that it intrinsically records quantitative molecular information. In a deep UV transmission image the intensity of a given pixel, I , and the intensity of the same pixel in a blank field of view, I_0 , together determine the optical density (OD) at that pixel, by the Beer-Lambert law typically used in spectroscopy. Interpreting deep UV OD image data is more challenging than interpreting spectroscopy data because the pathlength is determined by the height of the cell which varies with position and because protein and nucleic acid both contribute significantly to the measured OD in proportion to their concentrations (Caspersson, 1950):

$$OD_{\lambda}(x, y) = \varepsilon_{\lambda}^{protein} c^{protein}(x, y)l(x, y) + \varepsilon_{\lambda}^{nucleicacid} c^{nucleicacid}(x, y)l(x, y)$$

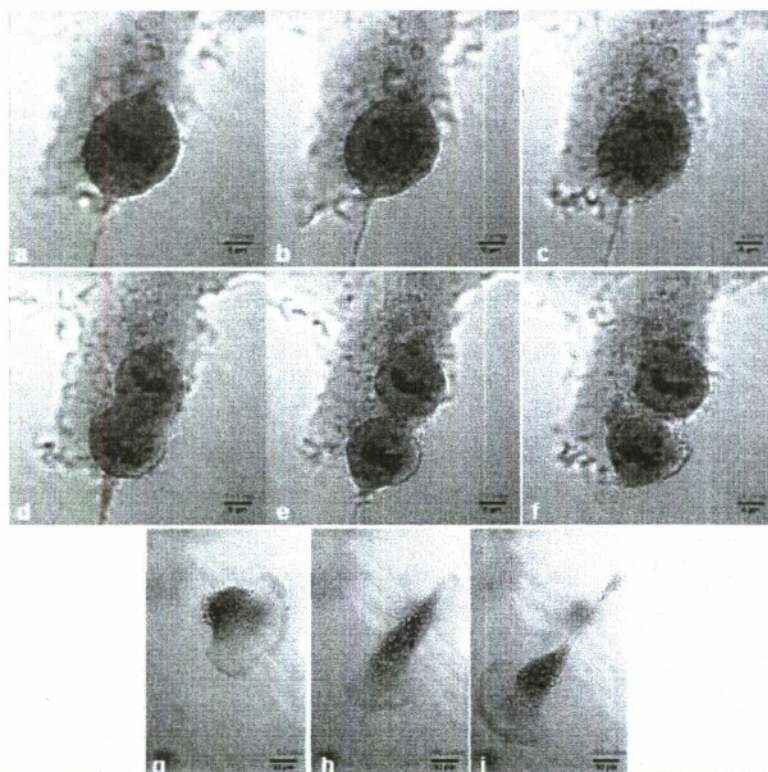
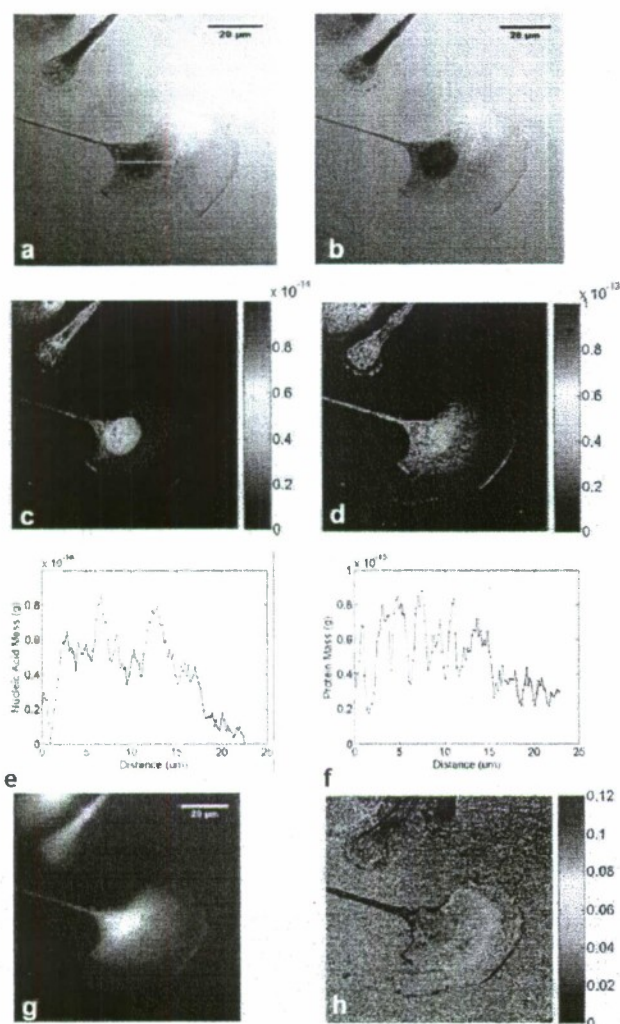


Fig. 5: Live-cell deep UV imaging. (A) Selected frames from time-lapse of HT-1080 (human epithelial fibrosarcoma) cell mitosis. (B) Selected frames from time-lapse of IC-21 cell motility.

where λ is wavelength, c is sample concentration, l is pathlength, and ϵ is the extinction coefficient. To determine the mass of protein and nucleic acid at each pixel, we acquire transmission images at both 280 nm (Fig. 6a) and 260 nm (Fig. 6b), as well as background images at both wavelengths. We estimate that $\epsilon_{260}^{\text{nucleic acid}} = 7,000 \text{ M}^{-1} \text{ cm}^{-1}$ by averaging known extinction coefficients for DNA and RNA at 258 nm, (Freifelder, 1982) and because pure nucleic acid has $\text{OD}_{260}/\text{OD}_{280} = 2.0$, (Gallagher, 2004) we estimate that $\epsilon_{280}^{\text{protein}} = 54,129 \text{ M}^{-1} \text{ cm}^{-1}$ and $\epsilon_{260}^{\text{protein}} = 36,057 \text{ M}^{-1} \text{ cm}^{-1}$ using the extinction coefficients for tryptophan, tyrosine, and phenylalanine at 260 nm ($3,787 \text{ M}^{-1} \text{ cm}^{-1}$, $582 \text{ M}^{-1} \text{ cm}^{-1}$, and $147 \text{ M}^{-1} \text{ cm}^{-1}$) and at 280 nm ($5,559 \text{ M}^{-1} \text{ cm}^{-1}$, $1,197 \text{ M}^{-1} \text{ cm}^{-1}$, and $0.7 \text{ M}^{-1} \text{ cm}^{-1}$) in neutral solution, (Fasman, 1990) an average 466 amino acid protein, (Lodish, 2004) and the tryptophan, tyrosine, and phenylalanine frequencies (1.4%, 3.2%, and 3.9%). (Voet, 1995) Inserting these values into the above equation for each wavelength yields two linear equations that together determine the values of $c^{\text{nucleic acid}} l$ and $c^{\text{protein}} l$ at each pixel. Multiplying these concentration-pathlength products by the area of each pixel yields the quantity of each in moles. Using an average molar mass of 52,728 Da for protein (Lodish, 2004) and of 330 Da for nucleic acid (Berg, 2002) yields the mass of each. Displaying this value at each pixel yields the nucleic acid mass (Fig. 6c) and protein mass (Fig. 6d) contained in the volume defined by that pixel projected through the cell, i.e. a nucleic acid map and a protein map. The values can also be plotted for a line section through the nucleus (Fig. 6e-f).

The maps show nucleic acid heavily concentrated in the nucleus with some in the surrounding area, while protein concentration is high in the nucleus but also throughout the cell and in the leading edge and tail. The line plots show sharp increases in protein



and nucleic acid at different points in the nucleus, which may indicate the presence of chromosomes and nucleoli as well as other structures. While the mass values are pathlength-independent, we can convert them to concentrations in mg/ml using an assumed pathlength $l = 8 \mu\text{m}$ for the nucleus. The concentrations then peak around 270mg/ml for protein and 27mg/ml for nucleic acid, values which compare favorably to published concentration estimates of protein (100-300mg/ml) and nucleic acid (26-46mg/ml).

Fig. 6: (a) 280nm and (b) 260nm transmission images, (c) Nucleic acid mass, (d) protein mass, (e) nucleic acid line plot, (f) protein line plot, (g) native fluorescence, and (h) quantum yield images.

Using a native fluorescence image (Fig. 6g) we can then calculate the quantum yield, q , of protein at each pixel. The protein mass map is critical for this calculation because it allows us to calculate the OD_{280} due to protein alone, independent of nucleic acid concentration. Protein quantum yield is commonly measured on proteins in solution to assay the molecular environment surrounding the fluorophore. The contribution of tryptophan is dominant in our native fluorescence images because the next strongest

fluorophore, tyrosine, is weaker, more easily quenched, (Freifelder, 1982) and has an emission maximum shorter than the 320 nm cut-on wavelength of our filter. The fluorescence intensity, I_{AF} , is determined by the equation:

$$I_{AF} = \left(\frac{T_{AF}}{T_{trans}} \right) \left(\frac{Eff_{AF}}{Eff_{trans}} \right) \frac{\sin^{-1} \left(\frac{NA}{n_{immersion}} \right)}{2 \cdot \pi} \cdot q \cdot I_O \cdot \left(1 - 10^{-OD^{tryptophan}} \right)$$

where T_{AF} and T_{trans} are the exposure times and Eff_{AF} and Eff_{trans} are the transmission efficiencies of the emission filters used for the native fluorescence and transmission images respectively, NA is the numerical aperture of the objective lens, $n_{immersion}$ is the refractive index of the immersion media, and q is the quantum yield. The optical density due to tryptophan, $OD^{tryptophan}$, can be calculated from four values in the previous paragraph: the $c^{protein}$ value, the average number of amino acids per protein, the average tryptophan frequency, and the tryptophan extinction coefficient at 280 nm. The I_O is the same for our transmission and fluorescence images since the microscope utilizes a diafluorescence arrangement, and can be determined from a transmission image of a blank field. Equation 2 then determines the quantum yield at each pixel, which can be displayed as a map (**Fig. 6h**). Published values of q for 20 isolated proteins (Fasman, 1990) have a mean of 0.125 ± 0.071 , while our q measurements cluster around 0.04. This difference may be caused in part by additional quenching in the closely packed environment of the cell, or by scattering effects which artificially inflate the measured protein mass.

Microscope Construction. An upright Axioskop microscope (Zeiss, Germany) was modified for 280 nm imaging. Continuous wave (CW) LEDs at 260 nm and 280 nm (Sensor Electronic Technology, Columbia SC) with specified output powers of ~0.2mW and ~1mW respectively and specified FWHMs of 11-12 nm were driven by an amplifier we constructed that was activated by a TTL output signal from the camera. Light was coupled into a UV multi-mode fiber (ThorLabs, Newton NJ), directed to a fused silica collector lens (Esco Products, Oak Ridge NJ), and focused by a UV-Kond condenser (Zeiss Germany) adjusted to 0.8 NA. A 100X Ultrafluor objective (Zeiss, Germany) was used. Transmission images were acquired using a bandpass filter in front of the camera with 50% transmission at 280 nm, better than 10% transmission from 260 nm - 291 nm, and 0% transmission at wavelengths longer than 295 nm (Chroma Technology Corp, Rockingham VT). Native fluorescence images were acquired with a longpass filter (Melles Griot, Irvine CA) with ~50% transmission at the cut-on wavelength of 320 nm and ~92% transmission at 360 nm and longer. In certain cases the light was focused by a quartz tube lens (Zeiss, Germany). A UV-sensitive PhotonMax CCD camera with a constant ~35% quantum efficiency from 200 nm-360 nm, rising to 60% at 400 nm and over 95% from 475 nm-700 nm was used, driven by WinView software (Princeton Instruments, Trenton NJ). Pixel sizes with and without the tube lens were determined using a fused silica Ronchi ruling (Edmund Optics, Barrington NJ). For some experiments a polarizing beam splitter cube (Newport, Irvine CA) with a different

collector lens directed part of the excitation to a UV-sensitive photodiode and this beamsplitter plus several waveplates slightly polarized the excitation, but any effects on the OD were insignificant. For live cell imaging the stage was heated by heating elements (Omega, Stamford CT) controlled by a thermostat controller (Minco, Minneapolis MN). For all experiments safety equipment and procedures were used to protect skin and eyes from UV exposure. For field search and focusing, a halogen lamp was connected to the fiber input in place of the LEDs. These wavelengths were found to be approximately parfocal with the deep UV wavelengths so that focus adjustment was unnecessary for live-cell imaging. To determine spatial resolution a set of NIST traceable polystyrene microspheres with a mean diameter of 205.6 ± 2.6 nm (Polysciences, Warrington PA) was imaged at various focal planes using both the 280 nm LED and the halogen lamp filtered with a 480 nm bandpass filter (Chroma Technology Corp, Rockingham VT) (Fig. 4).

Validation. We characterized solutions of purified tryptophan, protein, and nucleosides by imaging them in a $100\mu\text{m}$ width PDMS channel plasma-bonded to a quartz coverslip (Electron Microscopy Sciences, Hatfield PA). The channel was flushed with large volumes of purified water or PBS between readings. Solutions were measured on a spectrophotometer (NanoDrop Technologies, Wilmington DE) and in a fluorimeter (HoribaJobinYvon) before being imaged in the channel. Background images were obtained of the same channel filled with water or PBS, and the mean optical density/fluorescence values were determined in each case for a 200 pixel square towards the center of the channel. Solutions of L-Tryptophan (Sigma-Aldrich, St. Louis MO) were prepared at concentrations ranging from $\sim 0.5\text{mg/ml}$ to $\sim 4\text{mg/ml}$ in water and the results match well (Fig. 7). Solutions of Bovine Serum Albumin (BSA) (Sigma-Aldrich, St. Louis MO) in PBS at $\sim 124\text{ mg/ml}$, and adenosine (Sigma-Aldrich, St. Louis MO) (to simulate nucleic acid) in PBS at $\sim 2.4\text{ mg/ml}$ were mixed with ratios by volume of (4:0), (3:1), (2:2), and (1:3). The results for native fluorescence match the fluorimeter exceedingly well. The OD values also follow the right trends but are noisier because of the high absorbance of PDMS.

Cell Culture. Cells were grown at 37°C with 5% CO_2 . 1C-21 mouse macrophage cells

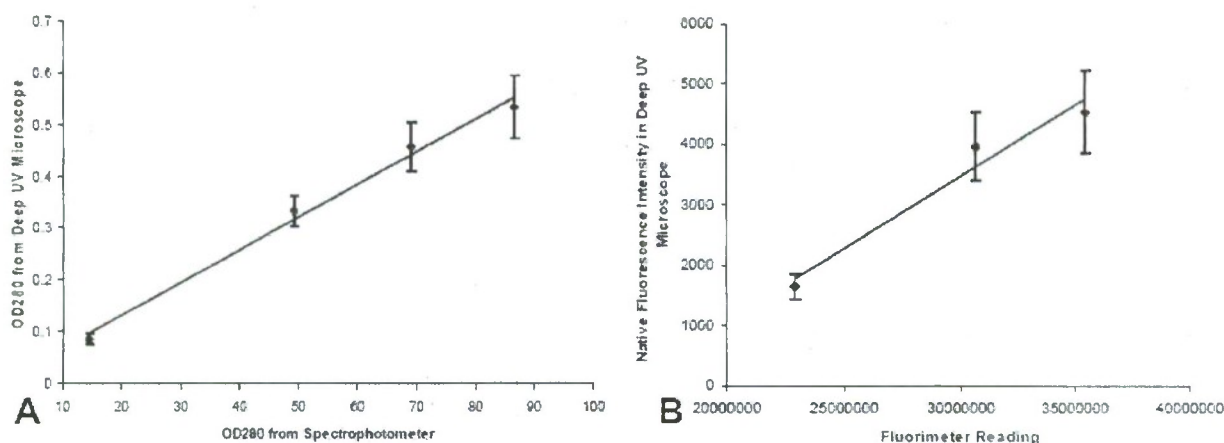


Fig. 7: Validation using tryptophan solutions. (a) OD280 for microscope versus spectrophotometer. (b) Fluorescence for microscope versus fluorimeter.

(ATCC, Manassas VA) were cultured in RPMI with ~1-2% penicillin-streptomycin (Mediatech, Herndon VA) and 15% FBS (Invitrogen, Carlsbad CA). HT-1080 human epithelial fibrosarcoma cells (ATCC, Manassas VA) were cultured in DMEM with 1% penicillin-streptomycin (Mediatech, Herndon VA) and 10% FBS. Cells were cultured on quartz coverslips (Chemglass, Vineland NJ; Electron Microscopy Sciences, Hatfield PA; Structure Probe, West Chester PA). For live cell imaging the coverslips were inverted onto a media-filled chamber made from an adhesive frame (Thermo-Electron Corp., Waltham MA) attached to a quartz slide (Chemglass, Vineland NJ.) warmed to 37°C.

Image Processing. ImageJ software (developed at NIH, freely downloadable) was used to set linear contrast display ranges, add scalebars and time stamps, select frames of interest from time series images, downsample to 8-bit for compatibility with word processing software, and in some cases rotate and/or crop. For movies it was used to create uncompressed avi files which were subsequently compressed with QuickTime Pro software (Apple Computer, Cupertino CA). Maps were calculated by MATLAB software (MathWorks, Natick MA) using the equations described in the text. Prior to calculation a mean offset ("dark value") of the camera was subtracted from the intensity of each intensity. For the protein and nucleic acid maps, the maximum displayed values were set to 1×10^{-13} g and 1×10^{-14} g respectively. The quantum yield map display range was set from 0 – 0.12.

Scattering Correction. The above method relies on the stated assumption that optical density equals absorbance. Since optical density measures extinction which can be caused by both absorbance and scattering, we have implicitly assumed that scattering effects are negligible.

Because the proteins solutions are relatively dilute, the same assumption of negligible is often made in spectroscopy studies, and scattering is rarely mentioned when spectra appear in literature associated with biological research. Nevertheless, several methods have been developed to characterize and correct for scattering effects in biological samples. Such corrections are important for imaging because measurements are made at much higher (10-1000X) protein concentrations.

Rayleigh Scattering Corrections in Literature. The magnitude of the extinction caused by scattering is a function of several factors including the size of the scattering particles and the wavelength λ of the incident light. In the limiting case when the particles are much smaller than the wavelength of the incident light, the extinction due to scattering is approximately proportional to λ^{-4} . This case is referred to as Rayleigh scattering. By measuring the optical density of a sample at wavelengths where it is known to have negligible absorbance, the optical density due to scattering at those wavelengths can be determined. Then, using the λ^{-4} relationship, the contribution to optical density from scattering can be calculated at wavelengths where there is significant absorbance.

As a demonstration of this technique, Freifelder uses the extinction of bacteriophage from 325 nm-400 nm to determine that the optical density due to scattering is 0.4 at 260 nm, roughly 7% of the total measured OD of 5.4 at this wavelength (Freifelder, 1982).

A slightly more robust way to characterize Rayleigh scattering assumes that the extinction due to scattering is approximately proportional to λ^{-n} , where $4 < n < 2$. Again, by measuring the optical density of a sample at wavelengths where it is known to have negligible absorbance, the optical density due to scattering at those wavelengths can be determined and the value of n extracted (Walker, 1956; Winder and Gent, 1971).

A third approach is described in a review and attributed to Moberger, who measured optical density of freeze-dried cells at 315 nm, and calculated the scattering at 265 nm using two relationships, λ^0 and λ^{-4} , which presumably represented the range of possible values (Walker, 1956). Interestingly, Moberger apparently found a much higher scattering contribution for freeze-dried cells than Freifelder did for bacteriophages – at a minimum about 20% of the total optical density at 265 nm. Writing at around the same time, Caspersson has yet another approach to the problem, conducting an extensive analysis of scattering from cells before concluding that it should not significantly influence absorbance measurements as long as the particles are larger than 3λ /(index of refraction) and other conditions are met such as the objective having a large numerical aperture (Caspersson, 1950).

Rayleigh Scattering Corrections for Imaging. Based on these approaches, we acquired transmission images of an IC-21 at 320 nm and 340 nm, wavelengths where there is negligible absorbance from protein and nucleic acid, in addition to 260 nm and 280 nm, and determined the OD at each wavelength. In order to extrapolate the contribution due to scattering at 280 nm and 260 nm, we first subtracted the OD340 from the OD320 value for a set of five images (more than 1.3 million pixels) but unexpectedly found that an average of 22% of the pixels had an OD340 value higher than the OD320 value, the opposite of the relationship expected from Rayleigh scattering. This suggested that a significant portion of the pixels did not experience major Rayleigh scattering, and so applying such a correction would introduce an unacceptably high amount of noise into our images.

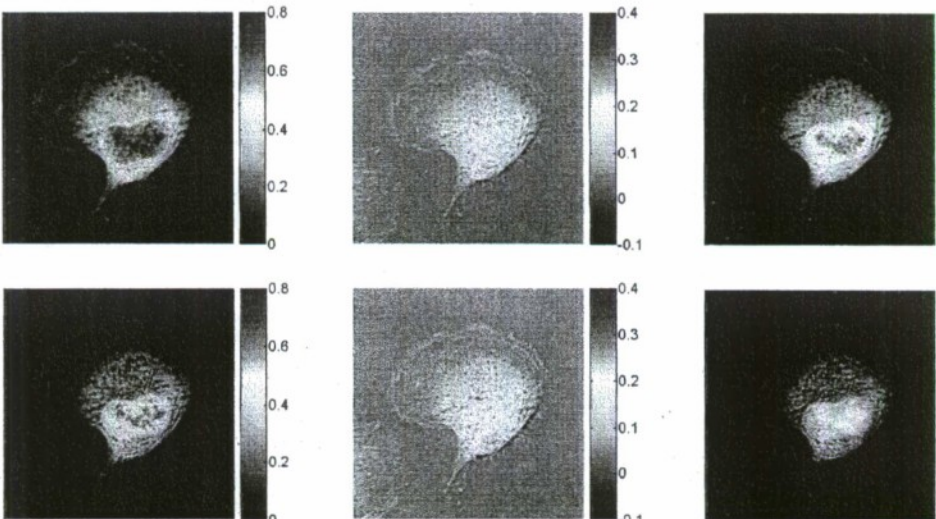
Mie Scattering Corrections for Imaging. The results from the previous section made it clear that the key assumption upon which the Rayleigh scattering equation was based, that the particles are much smaller than λ , was not accurate for a significant portion of our images. We then turned to the more general Mie scattering theory, using the Van de Hulst approximation for scattering cross section s_s as described in the literature (Perelman, 1998):

$$\sigma_s(\lambda, l) = \frac{1}{2} \cdot \pi \cdot l^2 \left[1 - \frac{\sin(2\delta/\lambda)}{\delta/\lambda} + \left(\frac{\sin(\delta/\lambda)}{\delta/\lambda} \right)^2 \right]$$

where $\delta = \pi \cdot l \cdot n_c(n-1)$, l is the diameter of the particles, n_c is the refractive index of the medium (cytoplasm) and n is the refractive index of the object. Substitution of the value for d yields:

$$\sigma_s(\lambda, l) = \frac{1}{2} \cdot \pi \cdot l^2 \left[1 - \frac{\sin(2\pi \cdot l \cdot n_c(n-1)/\lambda)}{\pi \cdot l \cdot n_c(n-1)/\lambda} + \left(\frac{\sin(\pi \cdot l \cdot n_c(n-1)/\lambda)}{\pi \cdot l \cdot n_c(n-1)/\lambda} \right)^2 \right]$$

According to another paper which also uses the Van de Hulst approximation, for a collimated beam the scattering coefficient μ_s can be determined by multiplying the scattering cross section by the number density of spheres N_s (Sefkow, 2001):



$$\mu_s = N_s \cdot \frac{1}{2} \left[\pi \cdot l \cdot n_c(n-1)/\lambda \left(1 - \frac{\sin(2\pi \cdot l \cdot n_c(n-1)/\lambda)}{\pi \cdot l \cdot n_c(n-1)/\lambda} \right) + \left(\frac{\sin(\pi \cdot l \cdot n_c(n-1)/\lambda)}{\pi \cdot l \cdot n_c(n-1)/\lambda} \right)^2 \right]$$

To convert the scattering coefficient μ_s to the more familiar ϵc value from the Beer Lambert law, we simply convert from natural log to log base ten by dividing it by 2.303:

$$\epsilon_{scattering} c = N_s \cdot \frac{1}{4.606} \cdot \pi \cdot l^2 \left[1 - \frac{\sin(2\pi \cdot l \cdot n_c(n-1)/\lambda)}{\pi \cdot l \cdot n_c(n-1)/\lambda} + \left(\frac{\sin(\pi \cdot l \cdot n_c(n-1)/\lambda)}{\pi \cdot l \cdot n_c(n-1)/\lambda} \right)^2 \right]$$

For the cytoplasm index of refraction we used a value of 1.35, and for the object index of refraction we used a value of 1.46 (Jacques, 1996). We wrote this equation in MATLAB (Mathworks, Natick MA) and used a nonlinear fit command to extrapolate the values of N_s and l that best fit our measured OD320 and OD340 values the values at each pixel. We then used these values to extrapolate a scattering correction for OD280 and OD260 and subtracted these from original OD values to produce corrected OD values (Fig. 8) which we then used to determine corrected protein and nucleic acid mass maps. It is likely that we will need to perform a similar scattering correction for images at 220 nm.

A Preliminary Polarization Modulator

We have developed a compact circular dichroism spectrometer. Current modulators are found in expensive instrument occupying over one meter of bench space. The size and cost of these instruments is primarily a function of three key components: a scanning detector, the light source, and polarization modulator. We have replaced the traditional light source with deep ultraviolet LEDs, which in turn enabled us to replace the traditional polarization modulator with a system that combines two orthogonally-polarized beams square-wave modulated 180 degrees out of phase. We have implemented this polarization modulation method using deep-UV LEDs, in order to detect CD in biological samples. This may lead to significant improvements in CD spectrometers and enable the integration of CD detection into a variety of sensors and imaging systems.

CD spectrometers typically generate light using a xenon lamp, which adds to the size, expense, and power consumption of the instrument and requires nitrogen purging. Lamp sources have been the only way to produce deep ultraviolet (UV) light, necessary because most biological molecules exhibit CD only at wavelengths between 200 – 300 nm. But recently, deep UV light-emitting diodes (LEDs) have come on the market, providing a small and inexpensive source of monochromatic deep UV.

Furthermore, instead of the photoelastic modulator (PEM) used in typical CD spectrometers, we have combine two orthogonally polarized beams square-wave modulated 180 degrees out of phase, to produce a single beam of light that oscillates between two orthogonal polarizations. This concept was suggested by Mackey et al.

Fig. 8: (left column) Original OD value, (middle column) calculated OD correction factor, and (right column) corrected OD value, for (top row) 260nm and (bottom row) 280nm.

(Mackey et al., 2002) for the measurement of birefringence. We have improved upon the Mackey concept by using square wave modulation instead of sinusoidal modulation to provide a stronger CD signal, by using deep UV LEDs instead of semiconductor lasers, and by adding a quarter-wave plate with its fast axis aligned 45 degrees from either of the orthogonal polarizations to produce light that oscillates between left and right circular polarization at a user-selectable frequency. The result is an extremely compact and inexpensive instrument capable of detecting CD at discrete deep-UV wavelengths (Fig. 9).

LED Driver Circuit

The LEDs were driven by a custom amplifier box built to our specifications. This has two driver outputs, one of which is inverted so that one of the LEDs is driven 180 degrees out of phase with the other. This circuit also has a TTL output that is used to synchronize the lock-in amplifier (Stanford Research Systems SR530) in order to measure the resulting signal. The output from the UV sensitive photodiode is amplified by a custom amplifier before being sent to the lock-in. The lock-in communicates with a computer via an RS232 connection where a QBASIC program is used to store the output data in a text file.

Beam Combination Methods

Implementing this polarization modulator setup requires combining the two beams. Initially, we attempted to do this using a Glan-Taylor

polarizer (ThorLabs), but this required injection of one of the beams at a 68° angle, which

proved difficult to align and implement. Our signal was improved by an order of magnitude when we replaced the Glan-Taylor polarizer with a sharp-edged mirror, so that one of the beams passed just by the edge, and the other beam reflected off it. This allowed us to have an orthogonal intersection which enabled much more consistent and rigid construction. Finally, for the microscope condenser assembly, we used a 90° polarizing beamsplitter cube from Newport.

In summary, we have developed and filed patents on an extremely compact device for detecting CD in biological samples using deep-UV light-emitting diodes and a polarization-modulation technique combining two orthogonally polarized beams square-wave modulated 180 degrees out of phase. While deep UV LEDs are currently available only at 247 nm and longer wavelengths, this number decreases steadily and we believe we will soon be able to implement this modulator with shorter-wavelength LEDs.

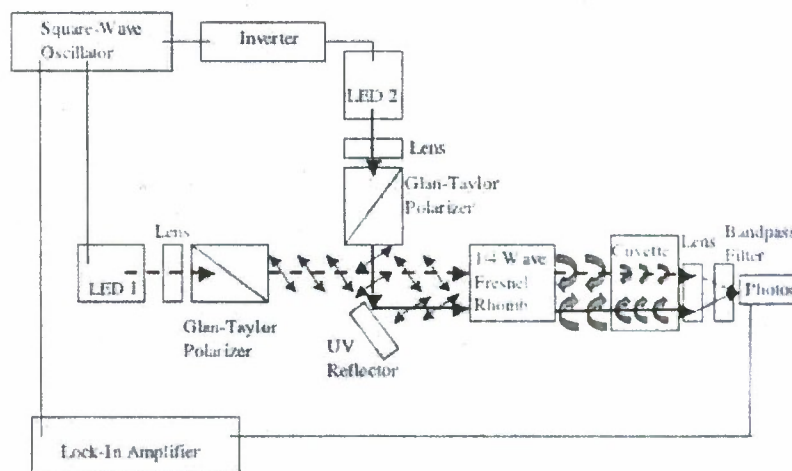


Fig. 9: Block diagram of our initial polarization modulator setup.

Preliminary 280 nm Polarization Imaging

We implemented the polarization combiner in the condenser as shown (Fig. 10), using a 266 nm polarizing beamsplitter cube (Newport 05SC16PC.22) in reverse as a polarizing beam combiner, held in a beamsplitter cube holder (Newport CH-0.5) with fused silica collector lenses (Esco Products) mounted in lens holders connected to the beamsplitter cube holder (Newport CH-PORT and MLH-0.5).

Conveniently, the threads on these holders also matched the threads from ThorLabs SM05 lens tubes, so we were able to add lens tubes and SMA fiber connectors directly. Above the beamsplitter holder we mounted a rotatable ThorLabs 266 nm zero-order half-wave plate and a fixed ThorLabs 266 nm zero-order quarter-waveplate. To verify the effectiveness of this arrangement, we utilized the long working distance of the Ealing 36X objective by placing a dichroic sheet polarizer (Oriel 27341) rated down to 270 nm between the sample and the objective. We then injected light into the bottom port and measured the average intensity of a blank image as a function of the half wave plate angle. Next we injected light into the side port and again measured average intensity of a blank image as a function of half-wave plate angle. The results are shown (Fig. 11) and

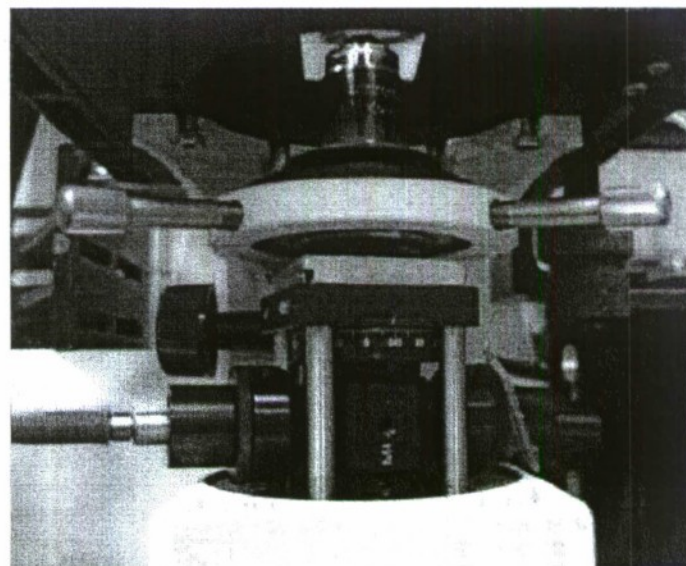
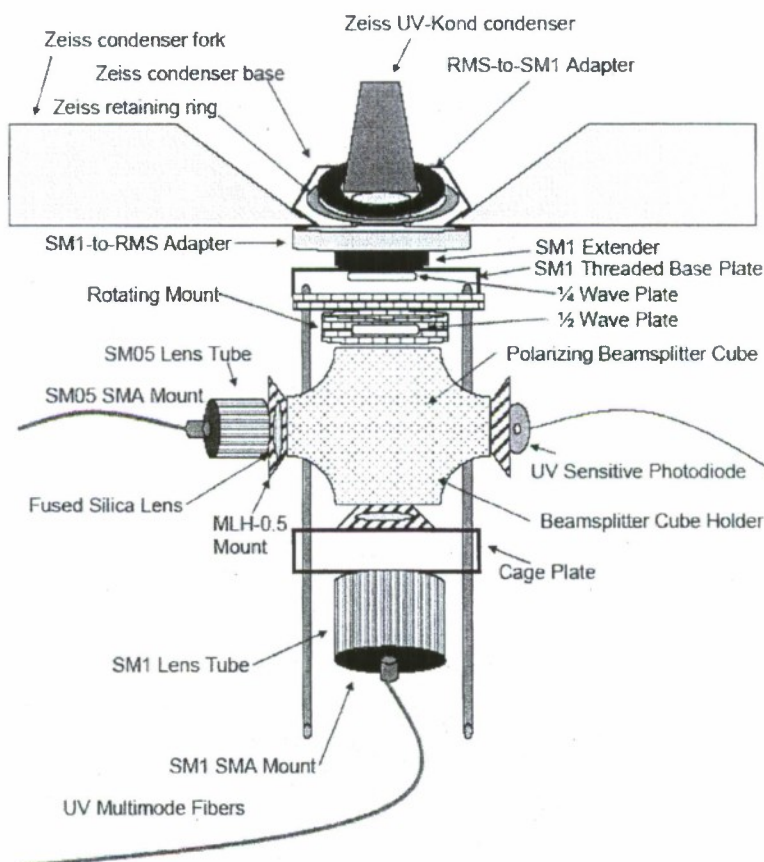


Fig.10: Diagram and photograph of our polarizing beam combiner condenser.

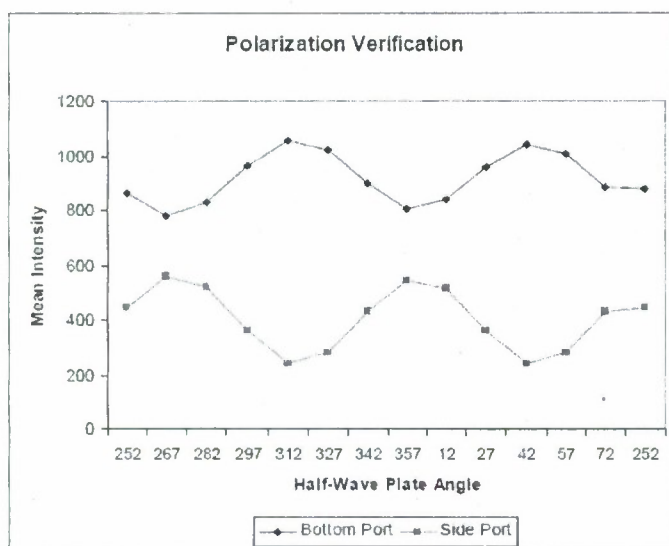
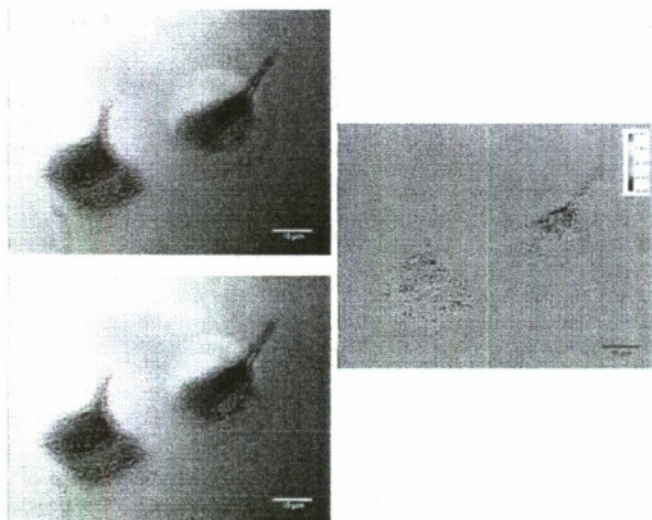


Fig.11: Verification of dual-port orthogonal polarizations.



Zeiss filter cube sliders to create a set of six different analyzer orientations in the emission pathway. The resulting traces intersect at approximately the same two half-wave plate angles as the previous calibrations, although this data is much noisier due in large part to imperfections in the polarizing film and mount.

280 nm Transmission Circular Dichroism Images

Our initial attempts to gather circular dichroism images occurred prior to the calibration for ideal half-wave plate rotation angle described in the previous section. Instead, we imaged CSA in a quartz microchannel, and water in a parallel quartz microchannel. For a variety of half-wave plate angles, we took images using both the

confirm that the condenser indeed produces orthogonally polarized beams. Next, we sought to determine the correct position of the half-wave plate in order to produce left and right circular polarization. To do this, we took advantage of the fact that when light is circularly polarized, a linear analyzer should yield the same intensity regardless of rotation angle. Again using the film polarizer mounted between the sample and the objective, we collected an array of images varying both the half-wave plate angle and the analyzer angle, and identified the two half-wave plate locations that most nearly produced the same intensity regardless of analyzer angle.

A similar calibration was not possible with the Ultrafluor objective due to its short working distance. Instead, we obtained 3M HNP'B film from American Polarizer which is rated as a linear polarizer at wavelengths as short as 280 nm. We cut six 25mm diameter circles from this film, and used a set of two

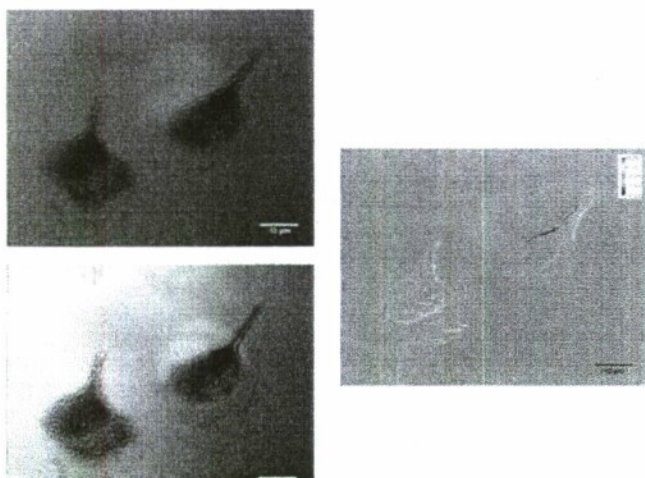


Fig.13: Attempted CD images of IC-21s by alternate use of side port and bottom port.

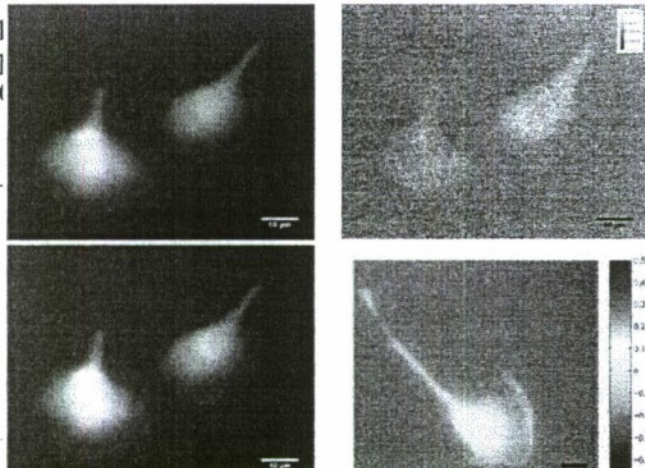
bottom and side ports in an attempt to acquire roughly circular polarizations of opposite handedness. However, these images seemed dominated by lensing at the edges, and even though there were some differences in signal between the water and CSA, it was extremely difficult to calibrate or draw any conclusions based on these images. We next tried sealing a small amount of CSA between a quartz slide and coverslip, but this also proved inconclusive, perhaps as a result of strain in the slide and coverslip.

After having identified the ideal half-wave plate angles for opposite circular polarizations as described in the previous section, we acquired images of cells with the half-wave plate at each position, determined the OD of each image, and used this to calculate the CD in mdeg (Fig. 12). We then acquired images of the same cells by keeping the half-wave plate in one fixed position, and directing the input through either the bottom port or the side port in order to get opposite handed circular polarizations. The results are shown (Fig. 13). The results from these two methods should match, but they do not yet. This fact, and the fact that we have been unable to effectively calibrate with CSA, illustrate that significant research effort is required to achieve effective CD imaging. We collected two consecutive same-handedness images and calculated the apparent circular dichroism caused by noise. There was a significant amount. One technical task in the development of a CD microscope is to inject the calibration camphorsulfonic acid into the scope.

280 nm Fluorescence-Detected Circular Dichroism Images

Using the exact same method of switching input polarization, and simply having a different emission filter, we measure the fluorescence-detected circular dichroism as shown (Fig. 14). These measurements are extremely high in noise and it is not clear if the signal exceeds the noise. It is necessary to develop ways to strengthen this signal.

Fig.11: Attempted CD images by manual rotation of $\frac{1}{4}$ wave plate. Left images taken with the $\frac{1}{2}$ wave



The image was calculated by dividing the difference of the two images by the sum of the two images, then multiplying by 2 using an equation from literature (Geng, 1994).

There is additional error because this measurement requires a manual rotation, and this also prevents it from being

automated for time-lapse images. We looked into acquiring a motorized rotator, but these are quite expensive. Another option may be to mount two differently oriented waveplates in a motorized filter wheel. But it would be ideal to use the modulator system, which would also improve the signal-to-noise ratio through synchronous detection.

Towards Circular Dichroism at Shorter Wavelengths

Our preliminary studies have encountered challenges because magnitude of the circular dichroism at 280 nm may be very small. It is also challenging to interpret circular dichroism at these wavelengths because the differences between different proteins are small and indistinct. Although CD spectra range from 190-300 nm, perhaps a useful wavelength is 222 nm, where strong signals and clear differences allow the differentiation of alpha helices and beta sheets. Much of the CD in proteins decreases to zero at wavelengths longer than 240 nm. Yet shorter than 240 nm, there is a significant amount of information and several quantitative methods to extract protein secondary structure from CD measurements (Venyaminov, 1996). Our research plan involves extending our preliminary studies of polarization modulation and circular dichroism

imaging to a range of wavelengths.

Fig. 14: Attempted FD CD images of IC-21s. (**top left and bottom left**) taken with the $\frac{1}{2}$ wave plate at each of the two angles determined to have circular polarization. (**top right**) Calculated CD from these two images by equations in the text. (**bottom right**) Another calculated FD CD image.